PAPER

Dual fluorescence properties and enhanced thermal stability of $SrSi_2O_2N_2$:Eu^{2+} phosphors by coupling with g-C_3N_4

Jinlong Wang,[a] Hao Song,[a] Peipei Dong,*[b] Zihan Zhao [ID][a] and Yanjie Zhang [ID]*[a]

Nowadays, considerable efforts have been extensively devoted to explore a general strategy for improving the color uniformity and thermal stability of phosphors, which is vital for its applications in health and comfort lighting. In this study, the $SrSi_2O_2N_2$:Eu^{2+}/g-C_3N_4 composites were successfully prepared *via* a facile and effective solid-state method to improve their photoluminescence properties and thermal stability. The coupling microstructure and chemical composition of the composites were demonstrated by high-resolution transmission electron microscopy (HRTEM) and EDS line-scanning analyses. Notably, the dual emissions at ∼460 nm (blue) and ∼520 nm (green) were observed for the $SrSi_2O_2N_2$:Eu^{2+}/g-C_3N_4 composite under near-ultraviolet (NUV) excitation, attributed to the g-C_3N_4 and 5d−4f transition of Eu^{2+} ions, respectively. The coupling structure will be beneficial to the color uniformity of the blue/green emitting light. Further, $SrSi_2O_2N_2$:Eu^{2+}/g-C_3N_4 composites exhibited a similar photoluminescence intensity compared with the $SrSi_2O_2N_2$:Eu^{2+} phosphor even after thermal treatment at 500 °C for 2 h due to the protection of g-C_3N_4. The decreased decay time (1798.3 ns) of green emission for SSON/CN compared with SSON phosphor (1835.5 ns) indicated that the coupling structure suppressed the non-radiative transition and improved photoluminescence properties and thermal stability. This work provides a facile strategy to construct $SrSi_2O_2N_2$:Eu^{2+}/g-C_3N_4 composites with coupling structure for improved color uniformity and thermal stability.

1. Introduction

White light emitting diodes (wLEDs), as the next generation of solid-state lighting sources, have been intensely studied in recent years due to their distinctive characteristics including high brightness, low power consumption, and brilliant stability.[1,2] The development of RGB (red, green, and blue) phosphors excited by near ultraviolet (NUV) LED chips has received much attention to achieve high-quality white light, which is highly corresponding to the requirement of health lighting. As the indispensable green component in wLEDs, Eu^{2+}-activated nitrides, and oxynitride phosphors, for example $SrSi_2O_2N_2$:Eu^{2+} green phosphors, have received close attention due to their high luminescent efficiency.[3,4] However, the thermal stability and anti-aging properties of nitrides and oxy-nitrides phosphors are inhibited due to the tendency of Eu^{2+} oxidation at high temperatures and high humidity.[5] In addition, the problems of reabsorption and color nonuniformity in the mixtures of tricolor phosphors limit their application in indoor lighting.[3] Therefore, it is an urgent task to explore a general strategy to improve both the color uniformity and thermal stability of phosphors.

The strategy of coating the particles with inorganic layers (*e.g.* SiO_2, C, SiC, Al_2O_3) can effectively improve the thermal stability of phosphors.[5–10] Yan *et al.* have prepared thermally stable $SrSi_2O_2N_2$:Eu^{2+} green phosphors by coating a thin carbon layer on the phosphor surface particles by the chemical vapor deposition (CVD) method.[7] Recently, major innovations in g-C_3N_4-based materials have emerged in large numbers for their excellent properties such as high photocatalytic activity, nontoxic nature, intense luminescence emission, and diverse access.[11,12] Actually, the research of carbon nitride (C_3N_4) can be traced back to 1834 when Liebig first obtained CN polymer and named it "melon".[13] Since then, the graphitic carbon nitride (g-C_3N_4) was reported by Franklin in 1922 through the thermal decomposition of mercuric thiocyanate.[14] In 1989, Liu and Cohen predicted the presence of ultra-hard material β-C_3N_4 by C replacing Si in the structure of β-Si_3N_4, theoretically.[15] In 1996, Teter and Hemley predicted five different phases of C_3N_4, which included α-C_3N_4, β-C_3N_4, c-C_3N_4, p-C_3N_4, and g-C_3N_4.[16] g-C_3N_4 has been widely used in several domains, such as photocatalysis,[17–19] solar energy conversion,[20,21] electro-catalysis,[22] illumination display[23,24] and biomedicine.[25] g-C_3N_4 can also be used as an optical material due to its unique energy-level structure, which is related to the transition between the

[a]*Research Institute of Photonics, Dalian Polytechnic University, Dalian 116034, China. E-mail: zhang_yj@dlpu.edu.cn*

[b]*College (Institute) of Integrative Medicine, Dalian Medical University, Dalian 116044, China. E-mail: dongpeipei11@163.com*

conduction band and valence band formed by the lone pair (LP) states of nitrogen.[26] Furthermore, g-C_3N_4, which improves the color uniformity of composite phosphors with an increased blue component in a coupled manner is widely available and non-dependent on the doping of rare earth ions. It can reduce the consumption of rare earth's finite resources on the planet for applying in white LEDs. Remarkably, tunable wavelength emission can be achieved by controlling the polymerization temperature of g-C_3N_4.[26,27] Further, the modified g-C_3N_4 phosphors indicate considerable potential for practical applications in optical materials due to their environmental friendliness, high quantum efficiency, and simple synthesis process.[28,29]

Thus, g-C_3N_4 is expected to improve the optical properties of the phosphor and keep it from thermal attack. Some researchers have combined g-C_3N_4 with long-afterglow phosphors, such as $SrAl_2O_4$, $CaAl_2O_4$, and $Sr_2MgSi_2O_7$, to achieve the photocatalytic activity in the dark environment and realize the purification of pollutants around the clock.[30–35] The combination of Ag_3PO_4/g-C_3N_4/$SrAl_2O_4$:Eu^{2+}, Dy^{3+} prepared by Lei et al. shows high photoactivity both under visible light irradiation and in complete darkness, which simultaneously enhances the photocatalytic activity for the phosphor-enriched composite when compared to pure g-C_3N_4.[32] There are two types of strategies to obtain composite phosphors based on g-C_3N_4. One of the strategies intends to improve the photoluminescence performance of the phosphor by compounding the phosphor with g-C_3N_4.[36–40] The $Y_3Al_5O_{12}$:Ce^{3+} phosphor with a thin g-C_3N_4 layer has been reported and exhibits the improved emission intensity, thermal stability, and quantum efficiency.[39] The purpose of another strategy is achieving white light by combing g-C_3N_4 with other red emission materials, such as Eu^{3+}:Y_2O_3, $Cu_3Cl(SR)_2$, $NaLuF_4$:Eu^{3+}, Ba_2MgWO_6:Eu^{3+}, and Eu^{3+}-doped molybdate phosphor, considering the blue emission at ~460 nm of g-C_3N_4 under near-UV excitation.[41–47] Guo et al. synthesized the new g-C_3N_4 composite red luminescent $Cu_3Cl(SR)_2$ composite phosphor with white light,[39] demonstrating that g-C_3N_4 is an excellent candidate material for improving phosphor performance and applying in NUV excited wLEDs.

In this work, a series of $SrSi_2O_2N_2$:Eu^{2+}/g-C_3N_4 composite phosphors have been prepared directly by facile thermal polymerization of melamine. The coupling structure and chemical composition of $SrSi_2O_2N_2$:Eu^{2+}/g-C_3N_4 composite were confirmed by HRTEM with EDS elemental analysis and FT-IR spectroscopy. The results from UV-vis diffuse reflectance spectra (DRS) indicated that the absorption capacity of the composite is improved and the optical band gap energy is reduced from 3.2 to 2.76 eV compared to those in $SrSi_2O_2N_2$:Eu^{2+}. The shift (from 370 to 448 nm) of the maximum excitation wavelength for $SrSi_2O_2N_2$:Eu^{2+}/g-C_3N_4 composite monitoring at 525 nm was found due to the decrease of the optical band gap. Under NUV excitation, the $SrSi_2O_2N_2$:Eu^{2+}/g-C_3N_4 composite exhibited the blue emission peak at ~460 nm and green emission peak at 525 nm corresponding to g-C_3N_4 and $SrSi_2O_2N_2$:Eu^{2+}, respectively. Further, it can be found that the thermal stability of the composite was improved and reached the maximum at a 5% molar mass ratio of g-C_3N_4. The mechanism of the improved photoluminescence properties and thermal

stability is attributed to the electron transfer from g-C_3N_4 to Eu^{2+} ions through the g-C_3N_4-$SrSi_2O_2N_2$ interface.

2. Experimental section

2.1 Materials and synthesis

The high-purity commercial chemical reagents used in this experiment are melamine (99%, A. R., Aladdin, China), $SrCO_3$ (99.9%, A. R., Aladdin, China), SiO_2 (99%, Sinopharm, China), α-Si_3N_4 (SN-E10, UBE Industries, Tokyo), and Eu_2O_3 (99.9%, Aladdin, China). All chemicals were of analytical grade or the highest purity available and were used without further purifications.

$SrSi_2O_2N_2$:Eu^{2+} phosphors were first prepared by a two-step solid-state reaction reported in our previous work.[48] A facile thermal polycondensation method was utilized to synthesize the $SrSi_2O_2N_2$:Eu^{2+}/g-C_3N_4 composite phosphors and pure g-C_3N_4. The raw materials of melamine and $SrSi_2O_2N_2$:Eu^{2+} phosphors were weighed stoichiometrically with various molar ratios and mixed thoroughly in an agate mortar. Then, the mixtures were transferred into an alumina crucible and calcined at 550 °C for 4 h in a tubular furnace under 3% H_2/N_2 reducing conditions. The yielded samples were denoted as X composites (X = 7/3, 3/2, 1/1, 2/3, 99/1, 97/3, 19/1, 9/1), where X refers to the molar ratio of $SrSi_2O_2N_2$:Eu^{2+}/g-C_3N_4. The yellowish fine powders were obtained after cooling down to room temperature and milled.

2.2 Characterizations

The crystal structure of the prepared powders was analyzed by X-ray diffractometer (XRD, Shimadzu, XRD-7000s) with Cu Kα radiation (λ = 1.54 Å) operating at 40 kV and 20 mA via diffraction patterns collected in the range from 10° to 70° at scanning speed of 5° per min. The particle morphology and structure of materials, as well as elemental distribution, were analyzed using a JEOL transmission electron microscope (TEM) equipped with an energy dispersion X-ray detector (EDX, X-Max 50, Oxford) and energy dispersive spectroscopy (EDS, JEM-2100F, JEOL). The microstructure of the composite phosphor was observed using a high-resolution transmission electron microscope (HRTEM) with a field emission tube in an accelerating voltage of 200 kV. Furthermore, the cross-section of the composite phosphor particles was performed by EDX line scanning in TEM. The specimens were dispersed into ethanol solution under ultrasonication for 20 min and a few drops were deposited on the copper grid before microscopic investigation. Fourier transform infrared spectroscopy (FTIR, Thermo Fisher Nicolet IS50) spectra were acquired to identify chemical groups in the samples in the range of 500–4000 cm^{-1}. UV-vis diffuse reflectance spectra (UV-vis DRS) of the composites were obtained using a UV-3600 spectrophotometer (Cary 100, Shimadzu, Japan). The spectra of photoluminescence (PL) and photoluminescence excitation (PLE) were measured on a fluorescence spectrophotometer (Hitachi, F-7000) at room temperature with an excitation source of a 200 W xeon lamp under a scanning rate of 240 nm min^{-1}. The emission spectra cover

the wavelength range of 400–650 nm under the excitation wavelength of 370 nm with an interval of 0.2 nm, and the slit width of excitation and emission was set to 1.0 nm. The decay time of $SrSi_2O_2N_2:Eu^{2+}$, $SrSi_2O_2N_2:Eu^{2+}$ after 500 °C thermal treatment ($SrSi_2O_2N_2:Eu^{2+}$-500) for 2 h, $SrSi_2O_2N_2:Eu^{2+}/g-C_3N_4$, and $SrSi_2O_2N_2:Eu^{2+}/g-C_3N_4$ after 500 °C thermal treatment for 2 h ($SrSi_2O_2N_2:Eu^{2+}/g-C_3N_4$-500) were measured under room temperature at the excitation and monitor wavelengths of 375 nm and 525 nm, respectively, on a lifetime spectrofluorometer (FLS980, Edinburgh Instruments) with a picosecond pulsed laser (EPL) of 375 nm. The thermal quenching was measured on Edinburgh Instruments (FLS 1000) at an excitation wavelength of 370 nm, with detection temperatures and ranges of 25–300 °C and 440–630 nm, respectively.

3. Results and discussion

3.1 Phase identification and microstructure analysis

Fig. 1 presents XRD patterns of pristine $g-C_3N_4$, $SrSi_2O_2N_2:Eu^{2+}$, $SrSi_2O_2N_2/g-C_3N_4$ composites (denoted as SSON/CN) and the standard data on the $SrSi_2O_2N_2$ crystal (JCPDS no. 14-8213). All the peaks of the as-synthesized $SrSi_2O_2N_2$ could be indexed using the reference card (JCPDS no. 14-8213), demonstrating that $SrSi_2O_2N_2:Eu^{2+}$ phosphor prepared by the two-step method exhibited the pure phase of $SrSi_2O_2N_2$. In Fig. 1, the intense peaks at 13.0° and 27.54° can be clearly observed for the diffraction of pristine $g-C_3N_4$, which is attributed to the (100) and (002) plane of the graphitic structure, respectively.[33] The diffraction peak at 13.0° is assigned to the intraplanar stacking of tri-s-triazine unit structures, while the major diffraction peak at 27.54° belongs to the interplanar packing of the conjugated aromatic systems of $g-C_3N_4$.[32] It can be clearly found from Fig. 1 that the diffraction peaks of SSON/CN composites are well-indexed to the $SrSi_2O_2N_2$ crystal (JCPDS no. 14-8213), but no

diffraction peaks of $g-C_3N_4$ were observed for SSON/CN composites even in the 2θ range of 25°-29° (right side, Fig. 1).

In order to investigate the $g-C_3N_4$ phase and microstructure, HRTEM images with elemental mapping of SSON/CN composites were performed and the data are shown in Fig. 2 and 3, respectively. Fig. 2a presents a TEM image of the SSON/CN composite prepared by molar ratio = 2/3, which clearly indicates the covering microstructure of the $g-C_3N_4$ layer on the surface of $SrSi_2O_2N_2:Eu^{2+}$ crystals with the average thickness in the range of 30–40 nm. In Fig. 2b, the lattice fringes of $g-C_3N_4$ with d spacings of 0.28 nm are shown for the SSON/CN sample, corresponding to the (102) crystal plane of $g-C_3N_4$ in the standard card data (JCPDS: 87-1526).[29] The corresponding energy dispersive X-ray spectroscopy (EDS) elemental mapping was also employed to further investigate the distribution of C, N, O, Si, Sr, and Eu elements for $SrSi_2O_2N_2:Eu^{2+}/g-C_3N_4$ composites. As shown in Fig. 3, all the elements of C, N, O, Si, Sr, and Eu appeared in the EDS spectrum and they were uniformly distributed throughout the phosphor particles.

Further, the elemental line scanning analysis was performed on the cross-section of SSON/CN particles and the arrow in the inset indicated the scanning direction in Fig. 4. Along the scanning direction (inset in Fig. 4), the signals of C, N, O, Si, Sr, and Eu elements can be found and increase to the maximum at the center of the particles. Therefore, the coupling structure of SSON/CN composites was demonstrated through HRTEM and EDS analysis, which will have a significant impact on the photoluminescence properties of the samples.

The combination of C_3N_4 with $SrSi_2O_2N_2$ was also investigated from FT-IR transmission spectra of $g-C_3N_4$, $SrSi_2O_2N_2:Eu^{2+}/g-C_3N_4$, and $SrSi_2O_2N_2$, as shown in Fig. 5. Fig. 5a presents the typical FT-IR spectrum of $g-C_3N_4$ with a broad absorption band localized at about 3000–3500 cm^{-1} attributed to the uncondensed terminal amino groups (–NH_2 or = NH groups).[36]
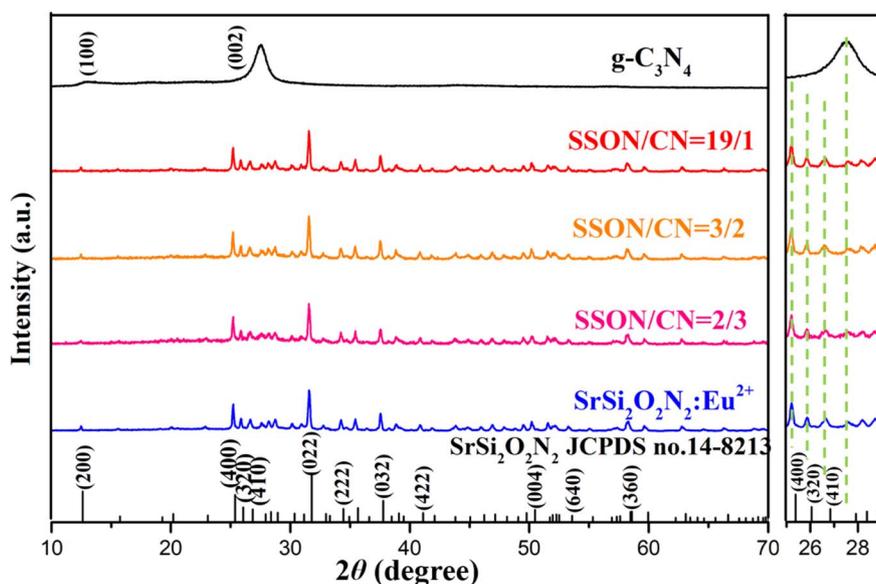

Fig. 1 XRD patterns of as-prepared pure $g-C_3N_4$, $SrSi_2O_2N_2:Eu^{2+}$, $SrSi_2O_2N_2:Eu^{2+}/g-C_3N_4$ composites (SSON/CN) with different molar ratios of SSON/CN and the standard data of $SrSi_2O_2N_2$ (JCPDS no. 14-8213).
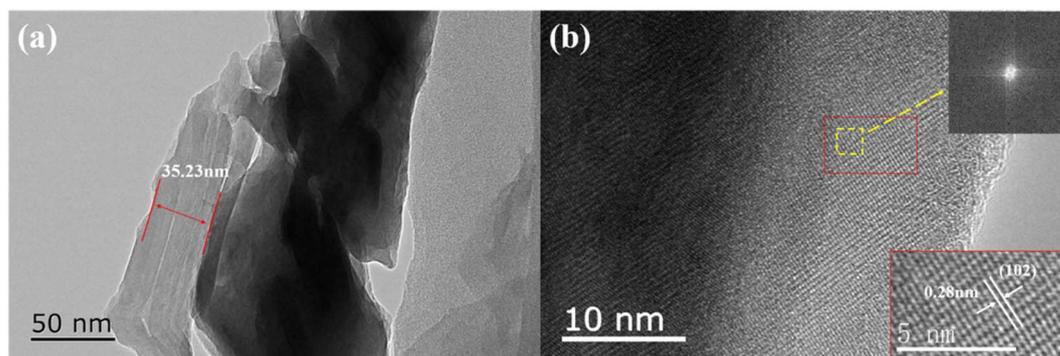
Fig. 2 (a) TEM image of SSON/CN sample prepared by molar ratio = 2/3. (b) HRTEM image of SSON/CN composite. The inset shows the FFT transform of the yellow region and the enlarged HRTEM image of the red area.

In the wavenumber range from 1200 to 1650 cm^{-1}, the absorption bands at 1564 and 1634 cm^{-1} are assigned to the stretching vibrations of C=N, while the bands at 1456, 1402, 1317, and 1244 cm^{-1} correspond to aromatic C–N stretching. In addition, the absorption peak at 807 cm^{-1} belongs to the triazine ring mode, attributed to the condensed CN heterocycle.[39,50] In Fig. 5c, the absorption peaks at 1024, 904 cm^{-1}, and

502 cm^{-1} are assigned to two Sr (Eu)–O (N) and Si–O (N) bonds in the SrSi$_2$O$_2$N$_2$:Eu^{2+} compound, respectively.[51] The peaks specified as the stretching and bending vibrations of O–H are located at about 3436 and 1630 cm^{-1}, respectively. Obviously, the FTIR spectrum of the SSON/CN sample with molar ratio = 2/3 shown in Fig. 5b exhibits the characteristic absorption peaks of SrSi$_2$O$_2$N$_2$ and C$_3$N$_4$. A broad absorption band at
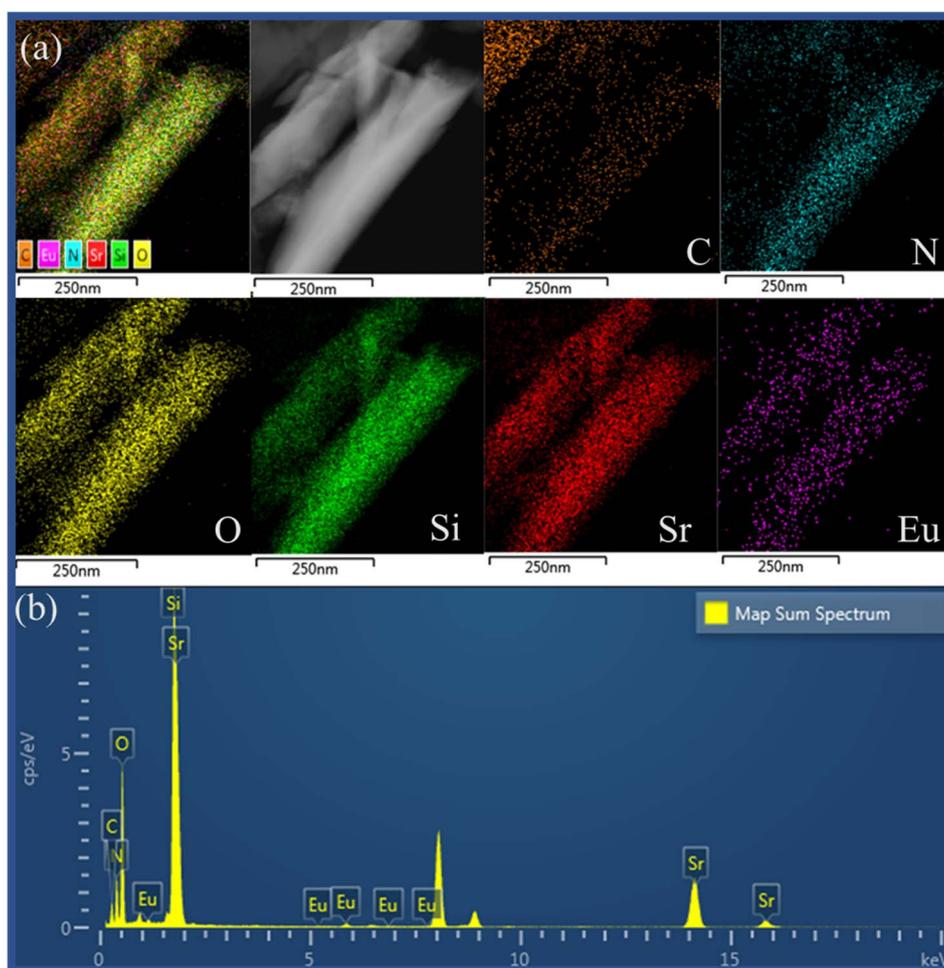

Fig. 3 (a) EDS mappings images of C, N, O, Si, Sr, Eu elements, and (b) EDS spectrum for SSON/CN sample prepared by molar ratio = 2/3.
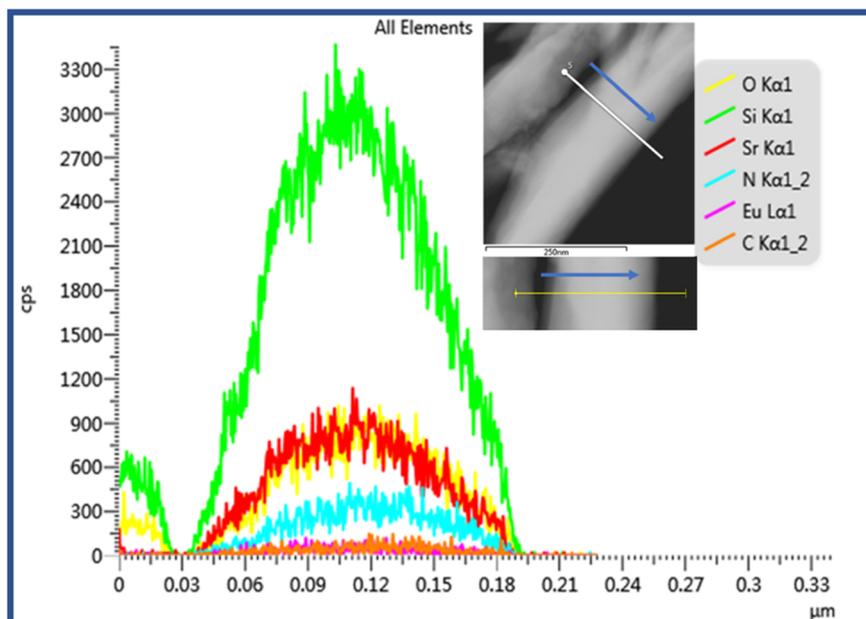
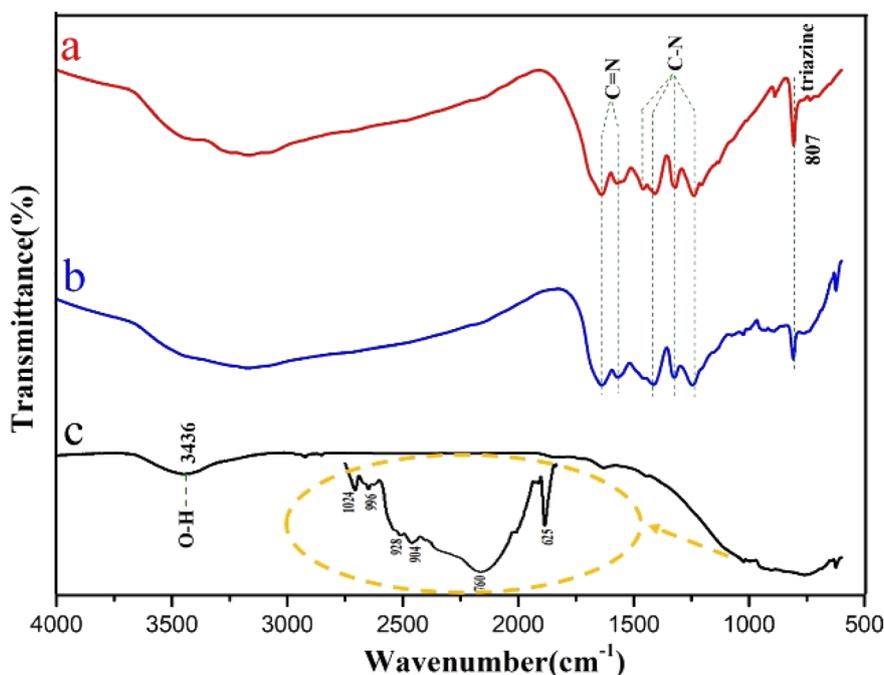**Fig. 4** EDS line-scanning analysis of SSON/CN sample with molar ratio = 2/3.

Fig. 5 FT-IR spectra of (a) pure g-C$_3$N$_4$, (b) SSON/CN sample with molar ratio = 2/3, and (c) SrSi$_2$O$_2$N$_2$:Eu^{2+}.

approximately 3170 cm^{-1} is attributed to the typical stretching vibration of O–H groups on the surface of the SrSi$_2$O$_2$N$_2$:Eu^{2+}/g-C$_3$N$_4$ composites.

3.2 Photoluminescence properties

It is necessary to evaluate the optical absorption of the samples before investigating the photoluminescence properties. Fig. 6a shows the UV-vis diffuse reflectance spectra (DRS) of g-C$_3$N$_4$,

SrSi$_2$O$_2$N$_2$:Eu^{2+}, and SSON/CN with strong absorption in the range of 200–450 nm. The obvious blueshift of the absorption edge from ~527 nm to ~471 nm can be found for SSON/CN composite phosphor when compared with SrSi$_2$O$_2$N$_2$:Eu^{2+}. The band gaps of g-C$_3$N$_4$, SrSi$_2$O$_2$N$_2$:Eu^{2+}, and SSON/CN were calculated using the Taucplot function:[32]

$$(\alpha h v)^n = K(h v - E_g)$$

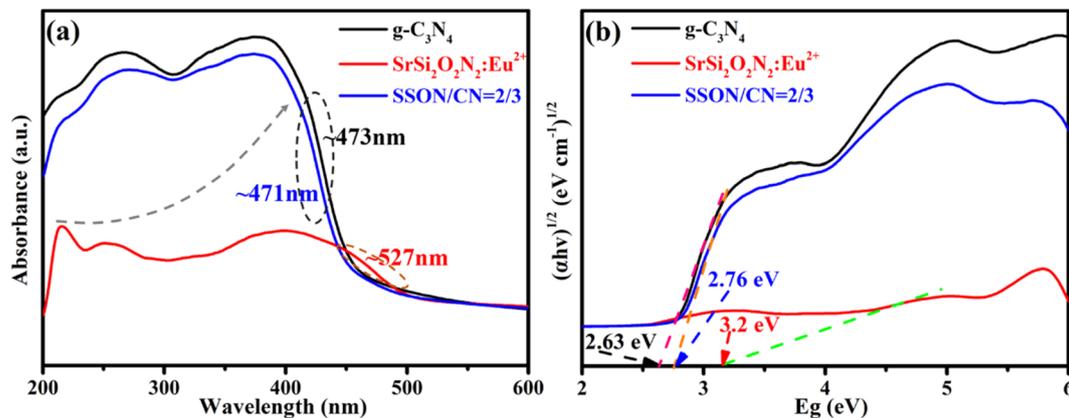**Fig. 6** (a) UV-vis diffuse reflectance spectra (DRS) and (b) Plots of $(\alpha h \nu)^{1/2}$ *versus hv* employed to determine the band gaps of g-C$_3$N$_4$ and SSON/CN composites phosphor. The molar ratio of SSON/CN was 2/3.

where α, h, ν, and K denote the absorption coefficient, Planck's constant, the frequency, and energy-independent constant, respectively. In addition, exponent "n" and "E_g" represent the nature of transition (direct or indirect band gap semiconductors) and the optical band gap energy, respectively. In Fig. 6b, the corresponding band gaps of g-C$_3$N$_4$, SrSi$_2$O$_2$N$_2$:Eu^{2+}, and SSON/CN were calculated to be 2.63 eV, 3.2 eV, and 2.76 eV, respectively. This change may be caused by the intra-band conversions of nitrogen-deficient porous g-C$_3$N$_4$ formed under H$_2$ mixing reduction atmosphere.[37]

Fig. 7 portrays the photoluminescence emission (PL) excited at 370 nm and the corresponding excitation (PLE) spectra of SrSi$_2$O$_2$N$_2$:Eu^{2+}, g-C$_3$N$_4$, and SSON/CN composites with the molar ratio of 2/3. As shown in Fig. 7a, the SrSi$_2$O$_2$N$_2$:Eu^{2+} phosphor exhibits a single broad green emission band peak at 525 nm with full width at half maxima (FWHM) of 61 nm, which is consistent with earlier reports of SrSi$_2$O$_2$N$_2$:Eu^{2+} phosphors.[48] The broad emission band in the range of 470–600 nm is associated with the transition from the lowest excited state of 4f^{6}5d^1 electronic configuration to the ground state 4f^7(^{8}S$_{7/2}$) of Eu^{2+} ions. Interestingly, g-C$_3$N$_4$ shows a broad blue emission band covering 400–550 nm and peaking at approximately 458 nm and

the FWHM of around 65 nm under the excitation of 370 nm, corresponding to near band edge emission (NBE) due to the direct bandgap transition in g-C$_3$N$_4$.[44] The optical properties of carbon nitride materials are mainly influenced by band-to-band transitions and band to tail transitions of lone pair (LP) states of intra-tri-*s*-triazine and inter-tri-*s*-triazine nitrogen, while the location of the LP band depends on the bond structure around the nitrogen.[26] As for SSON/CN composites, the PL spectra of SSON/CN shown in Fig. 7a exhibit blue-green dual emission peaks at 457 nm and 506 nm *via* Gaussian fitting under a single excitation wavelength (370 nm). A slight redshift from 458 nm to 463 nm can be observed for the SSON/CN composites compared with the emission of pure g-C$_3$N$_4$. The PL excitation spectrum of g-C$_3$N$_4$ in Fig. 7b displays a broad excitation band in the range of 250 to 430 nm. The strongest excitation bands are located at ~278 and 370 nm, which are attributed to π–π^* transitions and δ–π^* transitions, respectively.[26] Typically, the broad excitation peak of SrSi$_2$O$_2$N$_2$:Eu^{2+} phosphor covers the UV-visible region of 275–450 nm and the predominant excitation band appears at ~370 nm, relating to the parity allowed transitions from the 4f^7(^{8}S$_{7/2}$) to 4f^{6}5d^1 of the Eu^{2+} ions. The PLE spectrum consists of structural bands associated with the
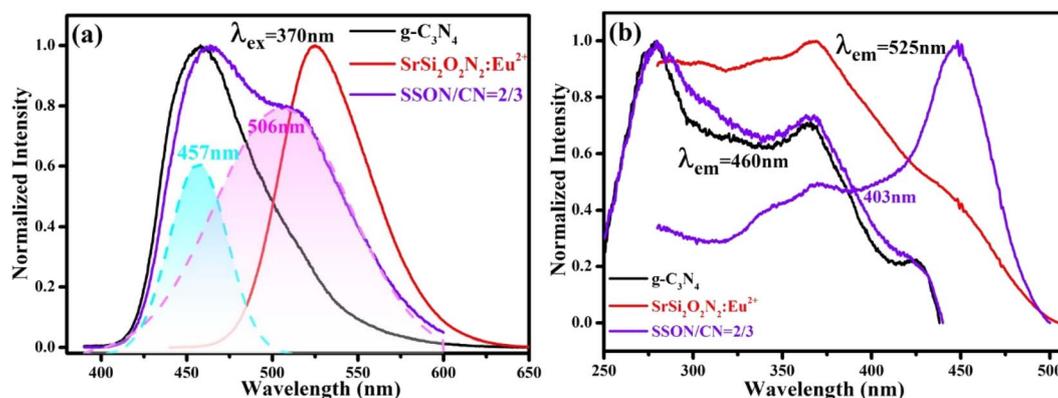

Fig. 7 Normalized PL emission (a) and excitation (b) spectra of SrSi$_2$O$_2$N$_2$:Eu^{2+}, g-C$_3$N$_4$, and SSON/CN with molar ratio 2/3. Dashed lines of (a) are Gaussian fitting of SSON/CN PL peak under 370 nm excitation.
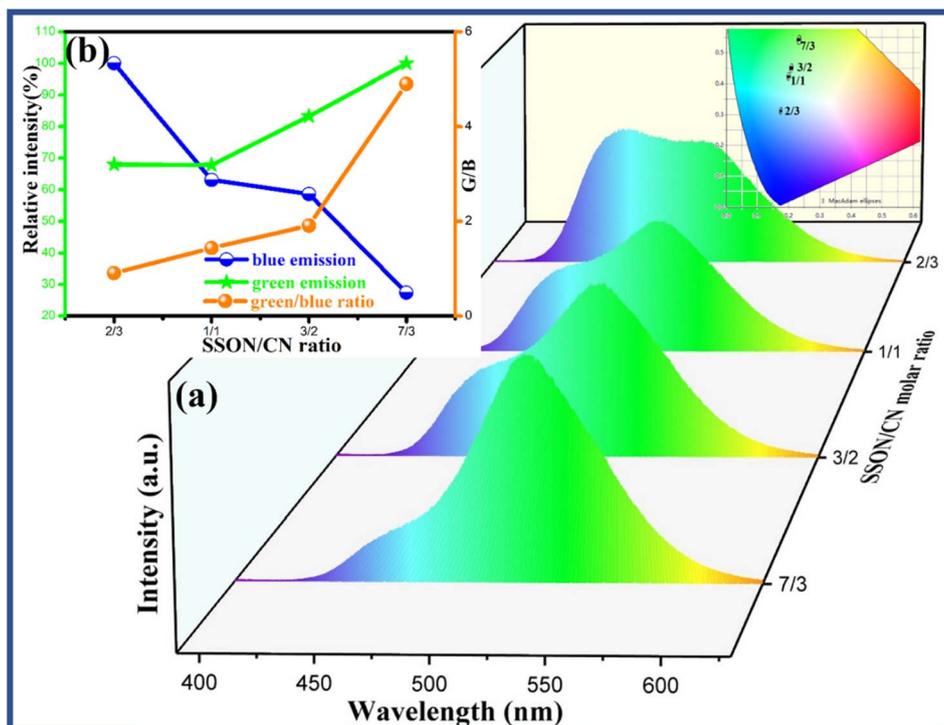
Fig. 8 (a) PL emission spectra of SSON/CN composites with different molar ratios (SSON/CN molar ratio = 7/3, 3/2, 1/1, and 2/3) prepared by thermal polymerization at 550 °C under excitation of 370 nm. Inset shows the CIE coordinates of the SSON/CN composite phosphors with different molar ratios. (b) The relative intensity variation of blue emission, green emission, and the corresponding green/blue ratio (G/B) with SSON/CN molar ratio.
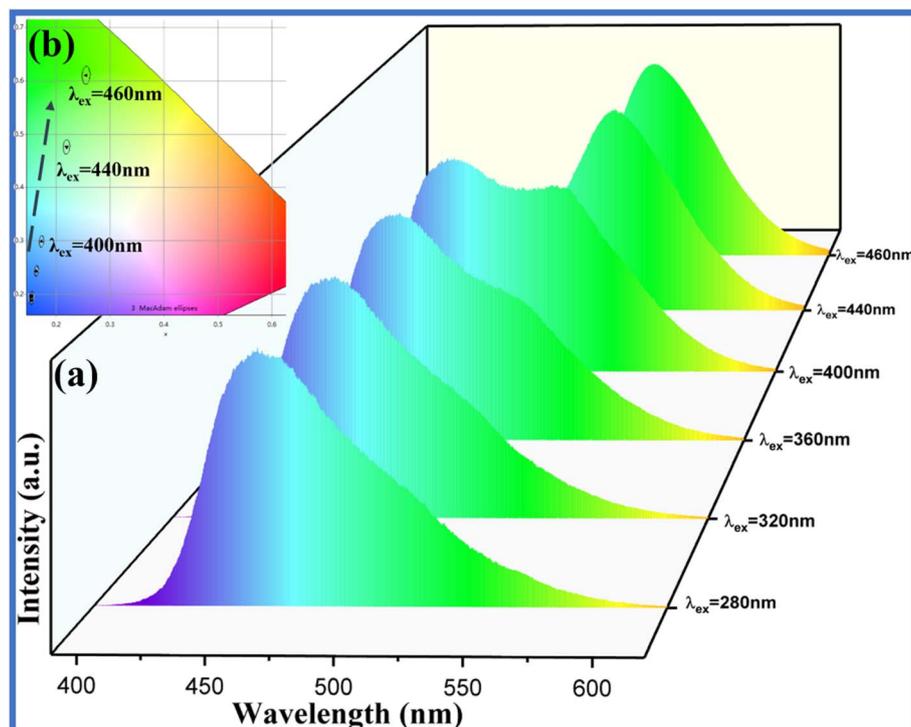

Fig. 9 (a) PL emission spectra of the sample prepared by SSON/CN molar ratio at = 2/3 under excitation of 280 nm, 320 nm, 360 nm, 400 nm, 440 nm, and 460 nm. (b) The coordinates of SSON/CN molar ratio at = 2/3 under different excitation wavelengths in CIE.

parity-allowed transition between the ground state and the excited states of the configuration of Eu^{2+} ions.[49] The PLE spectrum of the SSON/CN composites was recorded by monitoring the emission peak at 460 nm and 525 nm. The excitation band of SSON/CN composites monitored at 460 nm is similar to that from pure $g-C_3N_4$. Notably, it can be seen that the edge of the excitation band when monitoring the green emission at 525 nm dramatically extends to ~500 nm and shows the maximum excitation peak at ~450 nm, which is in accordance with the results of the UV-vis diffuse reflectance spectra shown in Fig. 6.

A series of SSON/CN composites with different molar ratios (SSON/CN molar ratio = 7/3, 3/2, 1/1, and 2/3) was prepared by thermal polymerization at 550 °C to investigate the photoluminescence properties under 370 nm excitation. It can be clearly noted from the PL emission spectra (Fig. 8a) of the composites under excitation of 370 nm that the samples display broad emission peaks in the range of 400–600 nm with a blue emission peak at ~460 nm and green emission peak at 525 nm corresponding to $g-C_3N_4$ and $SrSi_2O_2N_2:Eu^{2+}$, respectively. Along with the increase of $g-C_3N_4$ content in SSON/CN composites, the intensity of blue emission at ~460 nm increases and the CIE coordinates shift from (0.2339, 0.5416) to (0.1751, 0.3121) with the adjustable molar ratios, as shown in the inset in Fig. 8a. Fig. 8b displays the relative intensity

variation of blue emission, green emission and the corresponding green/blue ratio (G/B) with SSON/CN molar ratios. Obviously, the different green/blue ratios (G/B) from 0.5 to 4.5 can be facilely achieved by adjusting the SSON/CN molar ratios, which is helpful for its application in white light LEDs.

As shown in Fig. 9, the tunable proportion of blue and green emission can be facilely acquired by varying the excitation wavelengths (280 nm, 320 nm, 360 nm, 400 nm, 440 nm, and 460 nm, respectively). Obviously, the G/B ratios of the emission for $SrSi_2O_2N_2/g-C_3N_4$ composite with the molar ratio at = 2/3 can be adjusted to ~1 when employing the excitation wavelength of ~400 nm. Only the green emission peak for the as-prepared composite can be observed under excitation of 440 nm and 460 nm, due to the absence of absorption of $g-C_3N_4$ in this wavelength range. As shown in the inset of Fig. 9b, the coordinates in the CIE diagram shift from the blue region (0.1538, 0.1892) to the green region (0.2552, 0.6099) as the excitation wavelength increases. Thus, the dual emission of blue and green light can be achieved simultaneously in SSON/CN by manipulating the excitation wavelength.

3.3 Thermal stability of $SrSi_2O_2N_2:Eu^{2+}/g-C_3N_4$ composites

The thermal stability of phosphors plays a key role in the application of LED devices. Fig. 10a displays PL relative

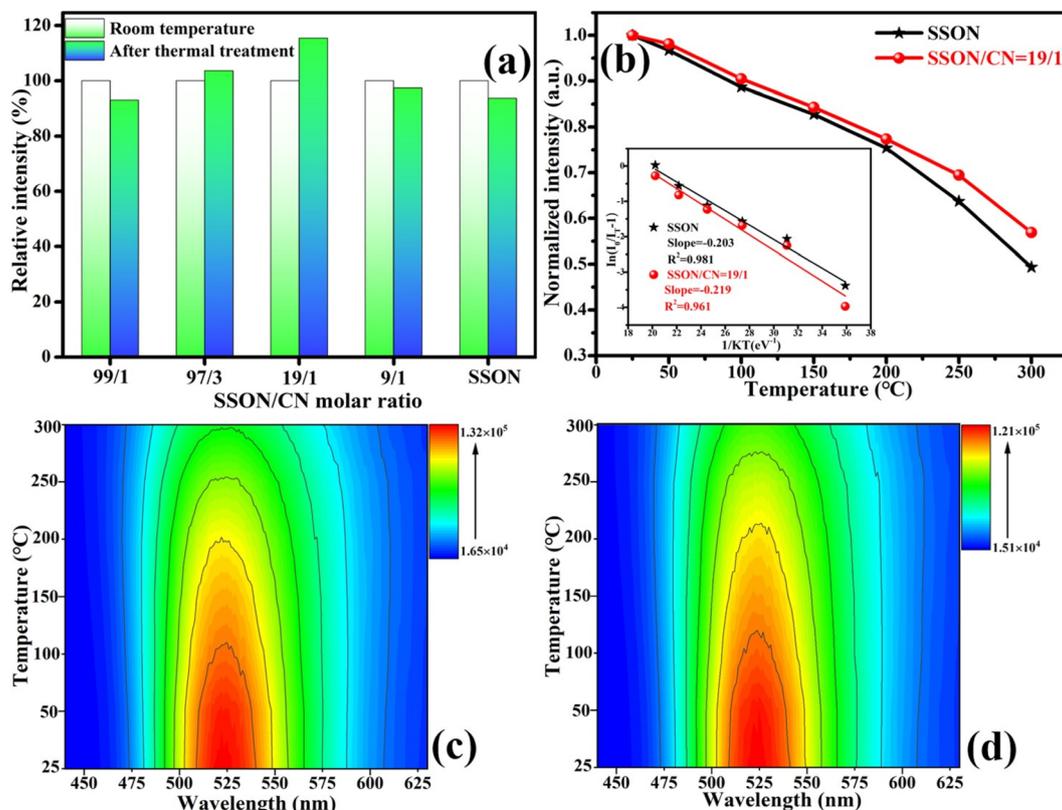**Fig. 10** (a) PL intensities of $SrSi_2O_2N_2:Eu^{2+}$, SSON/CN composites with different molar ratios (SSON/CN molar ratio = 99/1, 97/3, 19/1, and 9/1, respectively) and the corresponding samples after calcination at 500 °C for 2 h under excitation of 370 nm (All the measurements were conducted at room temperature). (b) Normalized PL intensities of $SrSi_2O_2N_2:Eu^{2+}$ and SSON/CN molar ratio = 19/1 as a function of temperature. The inset of (b) presents the Arrhenius plot to calculate the activation energy for thermal quenching of $SrSi_2O_2N_2:Eu^{2+}$ and SSON/CN molar ratio = 19/1. Temperature dependence of emission spectra of (c) $SrSi_2O_2N_2:Eu^{2+}$ and (d) SSON/CN molar ratio = 19/1.

emission intensities of $SrSi_2O_2N_2:Eu^{2+}$, SSON/CN composites with different molar ratios (SSON/CN molar ratio = 99/1, 97/3, 19/1, and 9/1, respectively) and the corresponding samples after calcination at 500 °C for 2 h under the excitation of 370 nm. Interestingly, SSON/CN composites with a molar ratio of 19/1 show abnormal fluorescence enhancement by 15.9% after calcination at 500 °C for 2 h, which is totally different from the decreased tendency of pure SSON phosphor after thermal treatment. In addition, the thermal quenching in Fig. 10b further demonstrates that the thermal stability of the SSON/CN composite is improved (molar ratio = 19/1). The activation energy is calculated using the Arrhenius formula.[39]

$$I_T = \frac{I_0}{1 + A e^{-\frac{\Delta E}{KT}}}$$

where I_0 and I_T represent the emission intensity at room temperature and at a given temperature, respectively. A, K, and ΔE represent the constant coefficient, Boltzmann's constant, and activation energy for thermal quenching, respectively. The graph of $\ln[(I_0/I_T) - 1]$ versus $1/KT$ was plotted and is shown in the inset of Fig. 10b. The ΔE was calculated as 0.203 and 0.219 eV for $SrSi_2O_2N_2:Eu^{2+}$ and SSON/CN, respectively. Fig. 10c and d show the temperature dependence of the emission spectra of $SrSi_2O_2N_2:Eu^{2+}$ and SSON/CN composite, respectively. The property parameters of $SrSi_2O_2N_2:Eu^{2+}$ and SSON/CN composites, upon thermal quenching, activation energy, and heating to 500 °C for 2 h and then dropping to room temperature, are shown in Table 1. The above observations indicated that the thermal stability can be effectively improved through coupling with $g-C_3N_4$. Thus, the coupling structure keeps the phosphor from thermal attack and subsequently improves the efficient electron transfer from $g-C_3N_4$ to Eu^{2+} ions.

The room-temperature decay curves were monitored at 525 nm under excitation of 375 nm for $SrSi_2O_2N_2:Eu^{2+}$, SSON/CN composite (molar ratio = 19/1), and the corresponding samples after 500 °C thermal treatment for 2 h, as shown in Fig. 11. All decay curves can be well fitted with double-exponential to equation $[I = I_0 + A_1 \exp(-t/\tau_1) + A_2 \exp(-t/\tau_2)]$, where I_0 is the initial luminescence intensity and I is the one at time t, A_1, and A_2 are the two constants of the function, τ_1, and τ_2 are the fast and slow components of the luminescent lifetimes, respectively.[36] Consequently, the average lifetime was calculated using the formula of $\tau^* = (A_1\tau_1^2 + A_2\tau_2^2)/(A_1\tau_1 + A_2\tau_2)$.[36,39] The average decay lifetimes were calculated as 1835.5, 1801.2, 1798.3, and 1820.5 ns for $SrSi_2O_2N_2:Eu^{2+}$, $SrSi_2O_2N_2:Eu^{2+}$-500, SSON/CN, and SSON/CN-500, respectively. Obviously, SSON/CN exhibits a decreased decay time (1798.3 ns) compared with

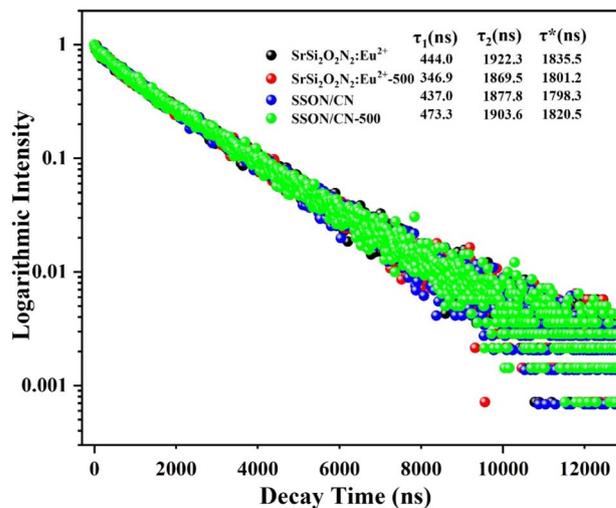**Fig. 11** Decay curves of $SrSi_2O_2N_2:Eu^{2+}$, SSON/CN composite (molar ratio = 19/1) and the corresponding samples after thermal treatment at 500 °C for 2 h. The samples were excited at 375 nm and monitored at 525 nm at room temperature.

SSON phosphor (1835.5 ns), indicating that the coupling structure suppressed the non-radiative transition and improved the photoluminescence properties.

3.4 Formation mechanism of SSON/CN composites

Fig. 12 illustrates the schematic diagram for the process for SSON/CN composites with dual fluorescence properties and enhanced thermal stability. Firstly, the SSON/CN composites were formed by the coupling of $SrSi_2O_2N_2:Eu^{2+}$ particles with stratified $g-C_3N_4$ through melamine thermal polycondensation. Under the excitation of 370 nm, SSON/CN composites exhibit dual photoluminescence emission peaks at 460 nm and 525 nm, assigned to $g-C_3N_4$ and 5d–4f transition of Eu^{2+}, respectively. The PL intensity and decay time of the as-prepared SSON/CN composite with SSON/CN molar ratio of 19/1 composite decrease slightly compared to that of $SrSi_2O_2N_2$:Eu^{2+} phosphor because the $g-C_3N_4$ layer can absorb the excitation light and facilitate the electron–hole recombination inside the layer. Notably, the PL intensity of the SSON/CN composite with SSON/CN molar ratio of 19/1 was increased by 15.9% after calcination at 500 °C for 2 h because of the coupling between $SrSi_2O_2N_2$ and $g-C_3N_4$. Simultaneously, the photo-generated carriers (electron–hole) during the thermal treatment process can be transferred to the luminescent center of Eu^{2+} ions in the

Table 1 The recently reported properties of $SrSi_2O_2N_2:Eu^{2+}$ phosphors

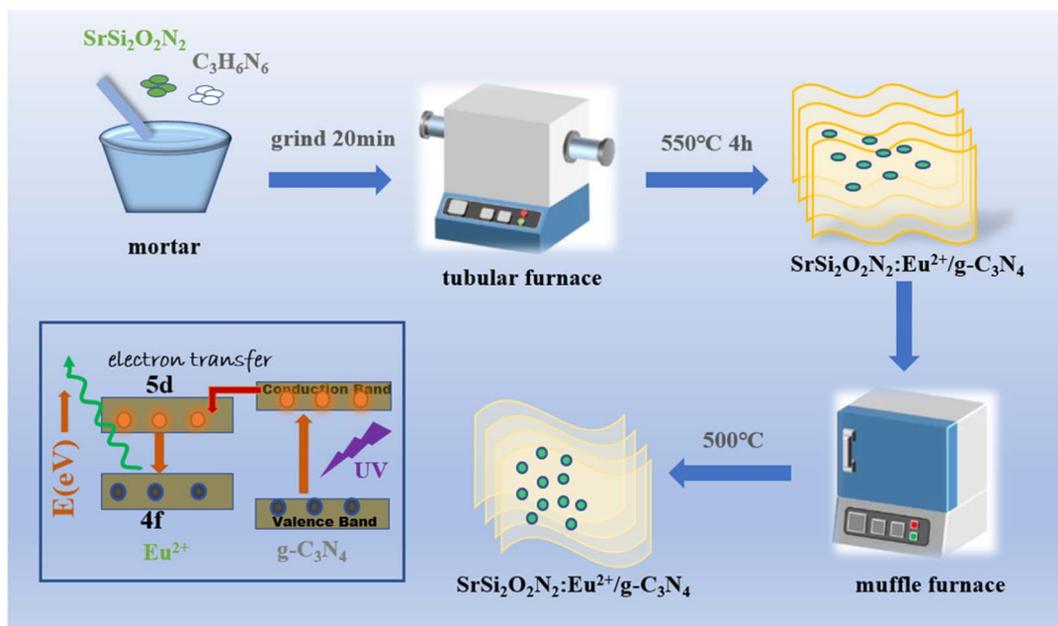| Phosphors	Excitation wavelength (nm)	Thermal quenching (remain)	Activation energy (eV)	Heated to 500 °C for 2 h	Ref.
$SrSi_2O_2N_2:Eu^{2+}$	370	74% (200 °C)	0.20	Decrease	This work
SSON/CN	370	78% (200 °C)	0.22	Increase	This work
$SrSi_2O_2N_2:Eu^{2+}$	380	85% (150 °C)	—	—	52
$Sr_{0.98}Si_2O_2N_2:0.02Eu^{2+}$	450	—	—	Decrease	53
$SrSi_2O_2N_2:Eu^{2+}$	440	71% (180 °C)	0.13	—	54

Fig. 12 Schematic diagram of the process for SSON/CN composites with dual fluorescence properties and enhanced thermal stability.

$SrSi_2O_2N_2$ lattice through the interface of $g\text{-}C_3N_4$–$SrSi_2O_2N_2$, demonstrated by the transient spectroscopy techniques (Fig. 11). Thus, the formation of the coupling structure of $g\text{-}C_3N_4$ coated on the surface of $SrSi_2O_2N_2:Eu^{2+}$ finally facilitated the color uniformity and improved thermal stability.

4. Conclusions

In summary, a series of SSON/CN composites were successfully synthesized by a facile thermal polymerization of melamine. The coupling structure of $g\text{-}C_3N_4$ coated on the surface of $SrSi_2O_2N_2:Eu^{2+}$ in the SSON/CN composite was confirmed by HRTEM with EDS analysis, which could have an essential impact on the color uniformity of the emitting light. The absorption spectra showed that the absorption ability of the composite was increased and the optical band gap energy was dropped from 3.2 eV to 2.76 eV when compared to that in $SrSi_2O_2N_2:Eu^{2+}$, which results in the redshift of the optimal excitation wavelength from 370 nm to 448 nm. The relative intensity of the blue-green emission can be controlled to improve the color uniformity of the SSON/CN composite by tuning different SSON/CN molar ratios and the excitation wavelength. The various green/blue emission ratios (G/B) from 0.5 to 4.5 can be obtained by the adjustment of SSON/CN molar ratios. Meanwhile, the SSON/CN composite exhibited higher thermal stability compared with the original $SrSi_2O_2N_2:Eu^{2+}$ phosphor from the thermal quenching results. The above results indicated that the preparation of composite phosphors is simple and effective, and has the potential to be extended to other phosphors for improving thermal stability. This work provides a simple and effective strategy to improve the color uniformity and thermal stability of nitride phosphor by constructing the coupling structure in $SrSi_2O_2N_2:Eu^{2+}/g\text{-}C_3N_4$ composites.

Conflicts of interest

There are no conflicts to declare.

Acknowledgements

References

1 S. Reineke, F. Lindner, G. Schwartz, N. Seidler, K. Walzer, B. Lüssem and K. Leo, *Nature*, 2009, **459**, 234–238.
2 S. Nakamura, T. Mukai and M. Senoh, *Appl. Phys. Lett.*, 1994, **64**(13), 1687–1689.
3 S. Xu, Y. Zhang, X. Wu, J. Wang, B. Li and J. Yu, *J. Alloys Compd.*, 2021, **875**, 160076.
4 C. Cai, W. Xie, L. Hao, X. Xu and S. Agathopoulos, *Mater. Sci. Eng. B*, 2012, **177**, 635–638.
5 D. Wu, L. Fu, S. He, F. Xu, L. Liu, L. Yao, F. Du, J. Peng and X. Ye, *Ceram. Int.*, 2020, **46**, 25382–25391.
6 J. Zhuang, Z. Xia, H. Liu, Z. Zhang and L. Liao, *Appl. Surf. Sci.*, 2011, **257**(9), 4350–4353.
7 R.-H. Yan, H. Ding, L. Gao, D.-Y. Chen, L.-W. Yin, A.-L. Xu, H.-L. Lv, X. Xu, L.-C. Ju and L.-J. Yin, *Mater. Chem. Phys.*, 2020, **256**, 123759.
8 L.-J. Yin, J. Dong, Y. Wang, B. Zhang, Z.-Y. Zhou, X. Jian, M. Wu, X. Xu, J. R. van Ommen and H. T. (Bert) Hintzen, *J. Phys. Chem. C*, 2016, **120**, 2355–2361.

9 G. Feng, W. Jiang, J. Liu, C. Li, Q. Zhang, L. Miao and Q. Wu, *Ceram. Int.*, 2018, **44**, 8435–8439.

10 Z. Chen, Y. Yan, J. Liu, Y. Yin, H. Wen, G. Liao, C. Wu, J. Zao, D. Liu, H. Tian, C. Zhang and S. Li, *J. Alloys Compd.*, 2009, **478**(1–2), 679–683.

11 M. Groenewolt and M. Antonietti, *Adv. Mater.*, 2005, **17**, 1789–1792.

12 X. Wang, K. Maeda, A. Thomas, K. Takanabe, G. Xin, J. M. Carlsson, K. Domen and M. Antonietti, *Nat. Mater.*, 2009, **8**, 76–80.

13 J. Liebig, Analyse der Harnsäure, *Ann. Pharm.*, 1834, **10**, 10.

14 E. C. Franklin, The ammino carbonic acids, *J. Am. Chem. Soc.*, 1922, **44**, 486–509.

15 A. Y. Liu and M. L. Cohen, *Science*, 1989, **245**, 841–842.

16 D. M. Teter and R. J. Hemley, Low-compressibility carbon nitrides, *Science*, 1996, **271**, 53–55.

17 S. Cao, J. Low, J. Yu and M. Jaroniec, *Adv. Mater.*, 2015, **27**, 2150–2176.

18 Q. Hao, G. Jia, W. Wei, A. Vinu, Y. Wang, H. Arandiyan and B.-J. Ni, *Nano Res.*, 2020, **13**, 18–37.

19 S. Lv, *et al.*, *Int. J. Hydrogen Energy*, 2021, **47**(100), 42136–42149.

20 X. Chen, Q. Liu, Q. Wu, P. Du, J. Zhu, S. Dai and S. Yang, *Adv. Funct. Mater.*, 2016, **26**, 1719–1728.

21 W.-W. Liu, Y.-C. Liu, C.-Y. Cui, S.-T. Niu, W.-J. Niu, M.-C. Liu, M.-J. Liu, B. Gu, L.-Y. Zhang, K. Zhao, F. Ran and Y.-L. Chueh, *Mater. Today Energy*, 2021, **21**, 100782.

22 J. Zhang, G. Zhang, X. Chen, S. Lin, L. Möhlmann, G. Dołęga, G. Lipner, M. Antonietti, S. Blechert and X. Wang, *Angew. Chem., Int. Ed.*, 2012, **51**, 3183–3187.

23 W. Liu, S. Xu, S. Guan, R. Liang, M. Wei, D. G. Evans and X. Duan, *Adv. Mater.*, 2018, **30**, 1704376.

24 L. He, M. Fei, J. Chen, Y. Tian, Y. Jiang, Y. Huang, K. Xu, J. Hu, Z. Zhao, Q. Zhang, H. Ni and L. Chen, *Mater. Today*, 2019, **22**, 76–84.

25 M.-H. Chan, R.-S. Liu and M. Hsiao, *Nanoscale*, 2019, **11**, 14993–15003.

26 Z. Gan, Y. Shan, J. Chen, Q. Gui, Q. Zhang, S. Nie and X. Wu, *Nano Res.*, 2016, **9**, 1801–1812.

27 Y. Zhang, Q. Pan, G. Chai, M. Liang, G. Dong, Q. Zhang and J. Qiu, *Sci. Rep.*, 2013, **3**, 1943.

28 T. Chen, C. Chen, Q. Liu, Z. Zhang and X. Fang, *RSC Adv.*, 2017, **7**, 51702–51710.

29 H. Li, F.-Q. Shao, H. Huang, J.-J. Feng and A.-J. Wang, *Sens. Actuators, B*, 2016, **226**, 506–511.

30 Y. Xiong, J. Zhao, Z. Zheng, F. Yi, X. Tang, D. jin and M. Jin, *J. Mater. Sci.: Mater. Electron.*, 2021, **32**, 7271–7284.

31 C. Zhou, P. Zhan, J. Zhao, X. Tang, W. Liu, M. Jin and X. Wang, *Ceram. Int.*, 2020, **46**, 27884–27891.

32 L. Lei, D. Wang, Y. Kang, Y. de Rancourt de Mimérand, X. Jin and J. Guo, *ACS Appl. Mater. Interfaces*, 2022, **14**, 11820–11833.

33 X. Liu, X. Chen, Y. Li, B. Wu, X. Luo, S. Ouyang, S. Luo, A. A. Al Kheraif and J. Lin, *J. Mater. Chem. A*, 2019, **7**, 19173–19186.

34 K. Hong, J. Hong and Y. Kim, *J. Photochem. Photobiol., A*, 2020, **396**, 112520.

35 X. Yang, B. Tang, X. Cao, Y. Ding and M. Huang, *J. Photochem. Photobiol., A*, 2021, **411**, 113202.

36 X. Jiang, S. Song, J. Guo, W. Lv, Y. Li, X. Guo, X. Wang, H. Liu, Y. Han and L. Wang, *Phys. Lett. A*, 2020, **384**, 126149.

37 Q. Dong, C. Guo, L. He, X. Yan and X. Lu, *Opt. Mater.*, 2020, **110**, 110527.

38 Y. Zhu, X. Li, B. Zhu and Y. Liang, *Inorg. Chem. Front.*, 2020, **7**, 3126–3135.

39 H.-R. Chen, C. Cai, Z.-W. Zhang, L. Zhang, H.-P. Lu, X. Xu, H. Van Bui, K.-H. Qiu and L.-J. Yin, *J. Alloys Compd.*, 2019, **801**, 10–18.

40 Y. Gong, Y. Liang, S. Liu, H. Li, Y. Bi, Q. Wang and Y. Dou, *Inorg. Chem. Front.*, 2021, **8**, 3760–3766.

41 S. Bayan, N. Gogurla, A. Midya and S. K. Ray, *Carbon*, 2016, **108**, 335–342.

42 P. Du, J. Tang, W. Li and L. Luo, *Chem. Eng. J.*, 2021, **406**, 127165.

43 J. Zhang, B. Han, P. Huang, J. Yu and L. Zhao, *Polyhedron*, 2017, **133**, 398–403.

44 H. Guo, J. Zhang, L. Ma, J. L. Chavez, L. Yin, H. Gao, Z. Tang and W. Chen, *Adv. Funct. Mater.*, 2015, **25**, 6833–6838.

45 B. Han, Y. Xue, P. Li, J. Zhang, J. Zhang and H. Shi, *J. Solid State Chem.*, 2015, **232**, 26–30.

46 B. Han, B. Liu, J. Zhang and H. Shi, *Optik*, 2017, **131**, 764–768.

47 Z. Zheng, Z. Zeng, Q. Guo, Q. Pan, J. Qiu and G. Dong, *J. Am. Ceram. Soc.*, 2020, **103**, 4411–4419.

48 W. Liang, Y. Zhang and M. Wang, *J. Lumin.*, 2019, **215**, 116646.

49 S. Mahlik, J. Barzowska, K. Szczodrowski, N. Majewska, M. Grinberg, D. Michalik, B. J. Adamczyk, T. Pawlik, T. Rzychoń, A. Adamczyk and M. Sopicka-Lizer, *J. Alloys Compd.*, 2021, **884**, 161047.

50 J. Xu, L. Zhang, R. Shi and Y. Zhu, *J. Mater. Chem. A*, 2013, **1**, 14766.

51 J.-Y. Tang, X.-F. Yang, C. Zhan, L.-Y. Hao, X. Xu and W.-H. Zhang, *J. Mater. Chem.*, 2012, **22**, 488–494.

52 L. Chen, Z. Cheng, G. Zheng, G. Yao, L. He, L. Wang, J. Liu, H. Zheng, S. Wei and H. Ni, *J. Lumin.*, 2021, **230**, 117729.

53 H. Wang, Z. Zhu, B. Ma, L. Wei and L. Li, *Ceram. Int.*, 2021, **47**, 24163–24169.

54 H. Li, H. Chen, L. Yang and M. Guo, *J. Lumin.*, 2018, **194**, 661–666.